Zhang *et al.*
Chinese Journal of Mechanical Engineering (2023) 36:58
https://doi.org/10.1186/s10033-023-00878-6

Chinese Journal of Mechanical Engineering

ORIGINAL ARTICLE

Open Access

An Energy Efficient Control Strategy for Electric Vehicle Driven by In-Wheel-Motors Based on Discrete Adaptive Sliding Mode Control

Han Zhang[1], Changzhi Zhou[1], Chunyan Wang[1] and Wanzhong Zhao[1*]

Abstract

This paper presents an energy-efficient control strategy for electric vehicles (EVs) driven by in-wheel-motors (IWMs) based on discrete adaptive sliding mode control (DASMC). The nonlinear vehicle model, tire model and IWM model are established at first to represent the operation mechanism of the whole system. Based on the modeling, two virtual control variables are used to represent the longitudinal and yaw control efforts to coordinate the vehicle motion control. Then DASMC method is applied to calculate the required total driving torque and yaw moment, which can improve the tracking performance as well as the system robustness. According to the vehicle nonlinear model, the additional yaw moment can be expressed as a function of longitudinal and lateral tire forces. For further control scheme development, a tire force estimator using an unscented Kalman filter is designed to estimate real-time tire forces. On these bases, energy efficient torque allocation method is developed to distribute the total driving torque and differential torque to each IWM, considering the motor energy consumption, the tire slip energy consumption, and the brake energy recovery. Simulation results of the proposed control strategy using the co-platform of Matlab/Simulink and CarSim® demonstrate that it can accomplish vehicle motion control in a coordinated and economic way.

Keywords Electric vehicle, Energy optimization, Motion control, Discrete adaptive sliding mode control

1 Introduction

Electric vehicles (EVs) have been considered as a substitution for the traditional vehicle with an internal combustion engine for the advantages of clean energy sources and emissions [1–3]. EVs driven by in-wheel-motors (IWMs) have been considered as a promising architecture for their noticeable advantages compared with other kinds of EVs [4, 5]. Firstly, the elimination of the transmission mechanism can save the producing cost and make more space for drivers and passengers. Secondly, the application of motorized wheels can improve motor-drive operation efficiency [6–8].

Besides the merits mentioned above, another significant advantage of EV driven by IWMs is that comprehensive performance can be elevated because the independent driving approach makes it possible to accomplish integrated optimization and control, then obtain more flexible responses under different driving conditions [9, 10]. Some prior researches have been done in this area. Yang et al. [11] proposed a current distribution control for dual directly driven wheel motors for EVs. They considered the status difference between two IWMs caused by fabricating qualities and different aging

*Correspondence:
Wanzhong Zhao
zhaowanzhong@126.com
[1] Vehicle Distributed Drive and Intelligent Wire Control Technology Research Center of Jiangsu Province, Nanjing University of Aeronautics and Astronautics, Nanjing 210016, China

rates and so on, and then developed an internal controller that serves to distribute the current, instead of torque, to the driving wheels, thereby enhancing the robustness and stability of the system. Demirci et al. [12] proposed a control method for IWM drive EV based on the direct yaw-moment control, giving the optimized wheel force distribution as well as the coordination control of the hydraulic braking and the motor torque, which improves the stability of the four-wheel-drive electric vehicle effectively. Wu et al. [13] presented a layered vehicle dynamic control system, which is composed of an adaptive optimal control allocation method using neural networks for optimal distribution of tire forces and the sliding mode yaw moment observer for robust control of yaw dynamics to solve the stability control problem. Hu et al. [10] utilized the front-wheel differential drive-assist steering to achieve path-following control for independently actuated electric autonomous ground vehicles. The differential torque between the left and right wheels can be utilized to actuate the front wheels as the sole steering power when the regular steering system fails, avoiding dangerous consequences.

Moreover, torque distribution, namely distributing the IWM torque properly to accomplish the given targets such as high dynamic demand, driving stability demand or good energy efficiency is also an important issue. A lot of reports on this subject and relevant studies have been published. Li et al. [14] presented an ideal force distribution control method for the EV based on the friction circle of tire force, making the front and rear wheels reach the adhesion limits at the same time in different conditions. Another optimal torque distribution for EV driven by IWMs was introduced by Zhang et al. [15]. The linear quadratic regulator via a weighted least square method was used to calculate the required longitudinal force of each wheel. Then the IWM torques were obtained by a tire slip ratio controller because they considered the longitudinal force of each wheel was decided by the tire slip ratio. To increase the cruising range of EVs equipped with front and rear in-wheel-motors, an optimal torque distribution algorithm for longitudinal motion by considering the transfer of weight between front and rear axles and motor losses was proposed by Wang et al. [16]. The EV was modeled as a linear-time-invariant system with generalized frequency variables and then the output power of IWM was modeled as a convex function of the distribution ratio, providing an added value for front-rear-independent-drive EVs. Li et al. [17] proposed a coordinated control algorithm of vehicle dynamics performance and energy consumption for an EV driven by four IWMs and steered by two steer-by-wire systems. In their study, multi controllers were designed for each subsystem at first and then a rule-based coordinated control scheme is developed according to vehicle driving states to accomplish the whole control target.

According to the abovementioned studies, an energy efficient control strategy for the electric vehicle driven by in-wheel-motors is designed in this paper. The overall control scheme is displayed in Figure 1. Different from previous research studies, we are aiming to obtain a good comprehensive vehicle performance in both dynamic motion control and energy efficiency. The overall control scheme consists of three parts. The first part is the vehicle motion controller using adaptive discrete sliding mode control (ADSMC) algorithm to calculate the longitudinal and yaw control efforts, guaranteeing good dynamics performance and stability. The second part is the lateral tire force estimation. Rather than linear tire force calculation, an unscented Kalman filter (UKF) is applied considering the tire nonlinear characteristics because the yaw moment is closely related to the tire lateral force, so precise estimation can contribute to further torque allocation. In the third part, the longitudinal and yaw control efforts will be distributed to each IWM considering the energy efficiency. More specifically, the optimal allocator is designed considering IWM energy consumption, tire slip energy consumption and brake energy recovery.

The rest of this paper is organized as follows. The vehicle nonlinear model and IWM model are built in Section 2, followed by the details about proposed control for IWM driven EV based on optimal torque allocation are presented in Section 3. Then the co-simulation results based on Matlab/Simulink and CarSim® are presented in Section 4, together with the related analyses. Finally, the conclusion will be summarized in Section 5.

2 Modeling

The vehicle nonlinear dynamic model, tire model and IWM model are constructed for further analysis and subsequent control strategy design.

2.1 Vehicle Dynamic Model

In this study, only longitudinal, lateral and yaw dynamics are concerned. A schematic diagram of the vehicle three degree-of-freedom nonlinear model [18] with four independently driven IWMs is shown in Figure 2.

The longitudinal, lateral and yaw motions of this model can be expressed as

$$\begin{cases} \dot{v}_x = v_y\gamma - F_w - F_f + \dfrac{1}{m}\sum F_x, \\ \dot{v}_y = -v_x\gamma + \dfrac{1}{m}\sum F_y, \\ \dot{\gamma} = \dfrac{1}{I_z}M_z, \end{cases} \tag{1}$$

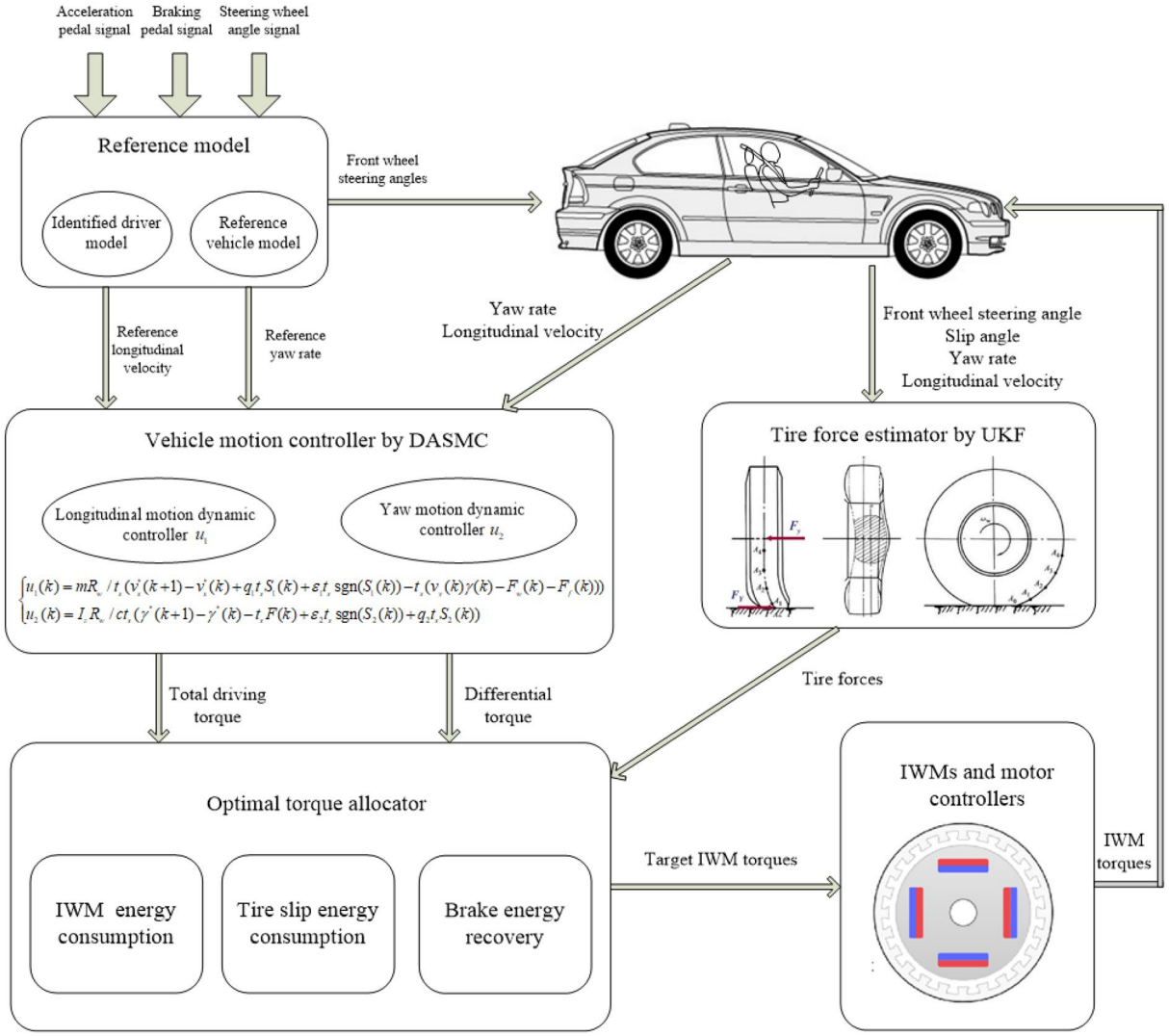

Figure 1 Energy efficient control strategy for EV driven by IWMs based on DASMC

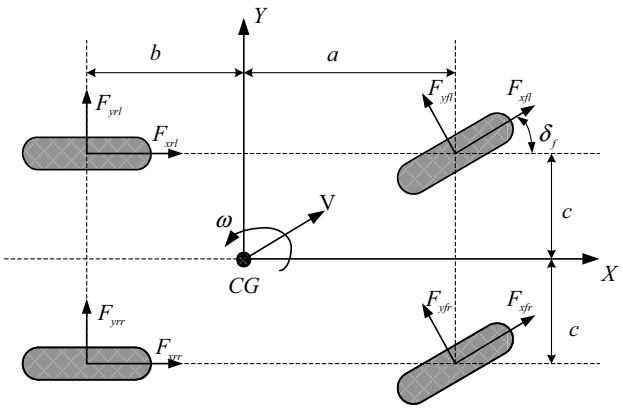

Figure 2 Schematic diagram of vehicle nonlinear model

where v_x, v_y and γ are the longitudinal velocity, lateral velocity, and yaw rate of the vehicle, respectively; m is the vehicle total mass; I_z is the vehicle yaw inertia; ΣF_x is the total longitudinal tire force; ΣF_y is the total lateral tire force; M_z is the total yaw moment provided by four wheels; F_w and F_f are the aerodynamic resistance and rolling resistance, respectively, which can be expressed as

$$F_w = \frac{1}{2} C_d \rho A v_x^2, \tag{2}$$

$$F_f = fmg, \tag{3}$$

where C_d is the aerodynamic resistance coefficient; ρ is the air density; A is the windward area; f is the rolling resistance coefficient; g is the gravity acceleration.

According to Figure 2, ΣF_x, ΣF_y and M_z can be written as

$$\begin{cases} \sum F_x = (F_{xfl} + F_{xfr})\cos\delta_f - (F_{yfl} + F_{yfr})\sin\delta_f + F_{xrl} + F_{xrr}, \\ \sum F_y = (F_{yfl} + F_{yfr})\cos\delta_f + (F_{xfl} + F_{xfr})\sin\delta_f + F_{yrl} + F_{yrr}, \\ M_z = c[(F_{xfr} - F_{xfl})\cos\delta_f + (F_{yfl} - F_{yfr})\sin\delta_f - F_{xrl} + F_{xrr}] \\ \quad + a[(F_{yfl} + F_{yfr})\cos\delta_f + (F_{xfl} + F_{xfr})\sin\delta_f] - b(F_{yrl} + F_{yrr}), \end{cases} \tag{4}$$

where δ_f is the steering wheel angle; F_{xi} is the longitudinal tire force of the ith wheel ($i = fl, fr, rl, rr$); F_{yi} ($i = fl, fr, rl, rr$) represents the lateral tire force of the ith wheel; a and b are the distances from the front and the rear axle to the center of gravity, respectively; c is half of the track width. The longitudinal tire force can be calculated by the wheel rotational dynamics equation, which is

$$\dot{\omega}_i = \frac{1}{I_w} T_i - \frac{R_w}{I_w} F_{xi}, \quad (i = fl, fr, rl, rr), \tag{5}$$

where T_i and ω_i are the driving torque and the angular speed of the ith wheel; I_w and R_w are the wheel moment of inertia and tire rolling radius, respectively. T_i is the ith IWM output torque.

2.2 Tire Model

The tire forces can be expressed by a Dugoff tire model [19] as follows

$$F_{xi} = \mu F_{zi} k_x \frac{\lambda_i}{1 + \lambda_i} f(L_i), \tag{6}$$

$$F_{yi} = \mu F_{zi} k_y \frac{\tan\alpha_i}{1 + \alpha_i} f(L_i), \tag{7}$$

$$f(L_i) = \begin{cases} (2 - L_i)L_i & L_i \le 1, \\ 1 & L_i > 1, \end{cases} \tag{8}$$

$$L_i = \frac{(1 - \lambda_i)(1 - \varepsilon v_x \sqrt{k_x^2 \cdot \lambda_i^2 + k_y^2 \cdot \tan^2\alpha_i})}{2\sqrt{k_x^2 \cdot \lambda_i^2 + k_y^2 \cdot \tan^2\alpha_i}}, \tag{9}$$

where k_x is the longitudinal stiffness; k_y is the lateral stiffness; μ is the road adhesion coefficient; α_i is the sideslip angle; λ_i is the longitudinal slip rate; F_{zi} is the vertical load of the tire. More specifically, α_i, λ_i and F_{zi} can be written as

$$\begin{cases} \alpha_{fl} = \alpha_{fr} = -\delta_f + \dfrac{a\gamma + v_y}{v_x}, \\ \alpha_{rl} = \alpha_{rr} = \dfrac{v_y - b\gamma}{v_x}, \end{cases} \tag{10}$$

$$\lambda_i = \frac{\omega_i R_w - v_i}{v_i}, \tag{11}$$

$$\begin{cases} F_{zfi} = (\dfrac{1}{2}mg + m\dfrac{a_y h}{c})\dfrac{b}{l} - \dfrac{1}{2}ma_x\dfrac{h}{l}, \\ F_{zfr} = (\dfrac{1}{2}mg - m\dfrac{a_y h}{c})\dfrac{b}{l} - \dfrac{1}{2}ma_x\dfrac{h}{l}, \\ F_{zrl} = (\dfrac{1}{2}mg + m\dfrac{a_y h}{c})\dfrac{a}{l} + \dfrac{1}{2}ma_x\dfrac{h}{l}, \\ F_{zrr} = (\dfrac{1}{2}mg - m\dfrac{a_y h}{c})\dfrac{a}{l} + \dfrac{1}{2}ma_x\dfrac{h}{l}. \end{cases} \tag{12}$$

2.3 IWM Model

Four permanent magnet synchronous motors (PMSMs) are applied as the driving motor [20]. Based on power invariant requirement, the d-q equivalent circuit of a PMSM is displayed as Figure 3.

In Figure 3, i_d and i_q denote the d- and q-axis components of armature current, respectively; u_d and u_q denote the d- and q-axis components of terminal voltage, respectively; R_a is the armature winding resistance per phase; R_c is the iron loss resistance; ϕ_f is the flux linkage generated by permanent magnets; L_d and L_q denote the d- and q-axis components of armature self-inductance, respectively; ω_e is the rotor angular velocity, ω_e=ω_{pn}; p_n is the number of pole pair.

The voltages of equivalent circuit are derived as

$$\begin{cases} u_d = R_a i_d - \omega_e L_q i_{qt}, \\ u_q = R_a i_q + \omega_e (L_d i_{dt} + \varphi_f). \end{cases} \tag{13}$$

The electromagnetic torque equation can be expressed as

$$T_e = p_n(\varphi_f i_{qt} + (L_d - L_q) i_{dt} i_{qt}), \tag{14}$$

where $L_d = L_q$ and the d-axis current can be controlled to be zero. Subsequently,

$$T_e = p_n \varphi_f i_{qt}. \tag{15}$$

Then the input power to a PMSM can be calculated by the following equation:

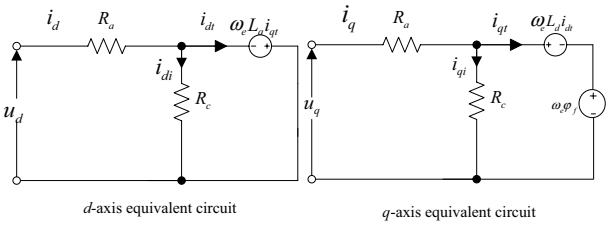

Figure 3 *D-q* equivalent circuit of a PMSM

$$\begin{aligned} P_{in} &= u_d i_d + u_q i_q \\ &= (R_a\, i_d - \omega_e L_q i_{qt}) i_d + (R_a i_q + \omega_e L_d i_{dt}) i_q \\ &= R_a\,(i_d^2 + i_q^2) + \omega_e^2 (L_d^2 i_{dt}^2 + L_q^2 i_{qt}^2)/R_c + \omega_e \varphi_f i_{qt}. \end{aligned} \tag{16}$$

3 Control Design for IWM Driven EV

The control method design is proposed in this section, including vehicle motion controller design, lateral tire force estimation and the optimal energy torque allocation.

3.1 Vehicle Motion Controller Design

Road interferences and parameter uncertainties are not considered in the modeling in Section 2. In order to preserve system stability as well as maintain good system robustness, the ADSMC is applied for vehicle motion control design [21].

Assuming $\sin\delta_f \approx \delta_f, \cos\delta_f \approx 1$, because of the small magnitude of front wheel steering angle, and substituting Eqs. (2)–(5) into Eq. (1), then Eq. (1) can be derived as

$$\begin{cases} \dot{v}_x = v_y\gamma + \dfrac{1}{mR_w}u_1 - F_w - F_f - d_1, \\ \dot{v}_y = -v_x\gamma + \dfrac{1}{m}(F_{yfl} + F_{yfr} + F_{yrl} + F_{yrr}), \\ \dot{\gamma} = a(F_{yfl} + F_{yfr}) - b(F_{yrl} + F_{yrr}) + \dfrac{c}{I_z R_w}u_2 + d_2, \end{cases} \tag{17}$$

where $u_1 = T_{fl} + T_{fr} + T_{rl} + T_{rr}$ and $u_2 = -T_{fl} + T_{fr} - T_{rl} + T_{rr}$ are the virtual control inputs to this nonlinear system; d_1 and d_2 are considered as modeling errors, which can be expressed as

$$d_1 = -\frac{I_w}{mR_w}(\dot{\omega}_1 + \dot{\omega}_2 + \dot{\omega}_3 + \dot{\omega}_4), \tag{18}$$

$$d_2 = \frac{I_w}{I_z R_w}(\dot{\omega}_1 - \dot{\omega}_2 + \dot{\omega}_3 - \dot{\omega}_4). \tag{19}$$

In real industrial applications, the control process is discrete. Furthermore, the real vehicle system is a nonlinear system and the longitudinal and yaw motion control problem proposed in our study is nonlinear. For these reasons, the discrete sliding mode control algorithm was adopted here. To reduce the chattering effect of discrete sliding mode control, the adaptive reaching law was introduced in the discrete sliding mode control. In summary, the most significant advantage of DASMC is that it can deal with the discrete nonlinear control problem and reduce the chattering effect of sliding mode control in the meantime. The vehicle model can be discretized as

$$\begin{cases} v_x(k+1) = v_x(k) + T_s(v_y(k)\gamma(k) \\ \qquad + \dfrac{1}{mR_w}u_1(k) - F_w(k) - F_f(k) - d_1(k))), \\ v_y(k+1) = v_y(k) + T_s(-v_x(k)\gamma(k) \\ \qquad + \dfrac{1}{m}(F_{yfl}(k) + F_{yfr}(k) + F_{yrl}(k) + F_{yrr}(k))), \\ \gamma(k+1) = \gamma(k) + T_s(a(F_{yfl}(k) + F_{yfr}(k)) \\ \qquad - b(F_{yrl}(k) + F_{yrr}(k)) + d_2(k) + \dfrac{c}{I_z R_w}u_2(k))), \end{cases} \tag{20}$$

The reference longitudinal velocity and yaw rate are defined as v_x^* and γ^*. Errors between the reference values and the actual values are given as $e_1 = v_x^* - v_x$ and $e_2 = v_\gamma^* - v_\gamma$. To realize $e_1 \to 0$ and $e_2 \to 0$, the sliding faces are defined as $S_1(k) = \rho_1 e_1(k)$ and $S_2(k) = \rho_2 e_2(k)$, where ρ_1 and ρ_2 are positive defined.

The Lyapunov function candidates are chosen as:

$$\begin{cases} V_1(k) = \dfrac{1}{2}S_1^2(k), \\ V_2(k) = \dfrac{1}{2}S_2^2(k), \end{cases} \tag{21}$$

and then

$$\begin{cases} \Delta V_1 = S_1^2(k+1) - S_1^2(k), \\ \Delta V_2 = S_2^2(k+1) - S_2^2(k). \end{cases} \tag{22}$$

According to the Lyapunov theorem of asymptotic stability, $S_j = 0, (j = 1, 2)$ is the system asymptotic stability surface, which means any starting state will eventually reach the switching surface $S_j = 0, (j = 1, 2)$. The reaching condition is taken as

$$S_j^2(k+1) < S_j^2(k),\ (j = 1, 2). \tag{23}$$

When sampling time t_s is small enough, the existing and reaching condition can be derived as

$$\begin{cases} [(S_i(k+1)-S_i(k)]\mathrm{sgn}(S_i(k)) < 0, \\ [(S_i(k+1)+S_i(k)]\mathrm{sgn}(S_i(k)) > 0, \end{cases} (j=1,2). \quad (24)$$

The exponential reaching law is chosen for this discretized sliding mode control problem, which is

$$\frac{S_i(k+1)-S_i(k)}{t_s} = -\varepsilon_i \mathrm{sgn}(S_i(k)) - q_i S_i(k), j=1,2, \quad (25)$$

where ε_j>0, q_j>0, 1−$q_j t_s$>0.

For Eq. (25), it can be derived as

$$\begin{aligned} &\left[S_j(k+1)-S_j(k)\right]\mathrm{sgn}\left(S_j(k)\right) \\ &= \left[-q_j t_s S_j(k) - \varepsilon t_s \mathrm{sgn}\left(S_j(k)\right)\right]\mathrm{sgn}\left(S_j(k)\right) \\ &= -q_i t_s \left|S_j(k)\right| - \varepsilon t_s < 0 \quad , j=1,2\,. \end{aligned} \quad (26)$$

Meanwhile, when sampling time t_s is small enough, $2-q_j t_s \gg 0$, then

$$\begin{aligned} &[(S_j(k+1)+S_j(k)]\mathrm{sgn}(S_j(k)) \\ &= [(2-q_i t_s)S_j(k) - \varepsilon t_s \mathrm{sgn}(S_j(k))]\mathrm{sgn}(S_j(k) \quad (j=1,2). \\ &= (2-q_i t_s)\left|S_j(k)\right| - \varepsilon t_s \left|S_j(k)\right| > 0, \end{aligned} \quad (27)$$

Thus, the reaching condition Eq. (23) can be achieved. Substituting Eq. (20) into Eq. (25), the control laws can be derived as

$$\begin{cases} u_1(k) = mR_w/t_s(v_x^*(k+1) - v_x^*(k) + q_1 t_s S_1(k) + \\ \quad \varepsilon_1 t_s \mathrm{sgn}(S_1(k)) - t_s(v_y(k)\gamma(k) - F_w(k) - F_f(k))), \\ u_2(k) = I_z R_w/ct_s(\gamma^*(k+1) - \gamma^*(k) - \\ \quad t_s F(k) + \varepsilon_2 t_s \mathrm{sgn}(S_2(k)) + q_2 t_s S_2(k)), \end{cases} \quad (28)$$

where

$$F(k) = a(F_{yfl}(k) + F_{yfr}(k)) - b(F_{yrl}(k) + F_{yrr}(k)) + d_2(k). \quad (29)$$

From Eq. (25),

$$S_j(k+1) = (1 - q_j t_s - \frac{\varepsilon_j t_s}{\left|S_j(k)\right|})S_j(k) = p_j S_j(k). \quad (30)$$

Then,

$$\left|p_j\right| = \frac{\left|S_j(k+1)\right|}{\left|S_j(k)\right|}, p_j = 1 - q_j t_s - \frac{\varepsilon_j t_s}{\left|S_j(k)\right|}. \quad (31)$$

Based on Eq. (31), there are three circumstances: ① when $\left|S_j(k)\right| > \varepsilon_j t_s / (2-q_j t_s)$, there is $p_j > 1 - q_j t_s - \varepsilon_j t_s(2-q_j t_s)/\varepsilon_j t_s = -1$, then $\left|p_j\right| < 1$, $\left|S_j(k+1)\right| < \left|S_j(k)\right|$, which means $\left|S_j(k)\right|$ is decreasing; ② when $\left|S_j(k)\right| < \varepsilon_j t_s / 2 - q_j t_s$, there is $p_j < 1 - q_j t_s - \varepsilon_j t_s(2-q_j t_s)/\varepsilon_j t_s = -1$, then $\left|p_j\right| > 1$, $\left|S_j(k+1)\right| > \left|S_j(k)\right|$, which means $\left|S_j(k)\right|$ is increasing; ③ when $\left|S_j(k)\right| = \varepsilon_j t_s / (2-q_j t_s)$, there is $p_j = 1 - q_j t_s - \varepsilon_j t_s(2-q_j t_s)/\varepsilon_j t_s = -1$, which means $\left|S_j(k)\right|$ is chattering. Thus, it can be concluded that the sufficient condition of $\left|S_j(k)\right|$ decrease is $\left|S_j(k)\right| > \varepsilon_j t_s / (2-q_j t_s)$. To achieve this, it is required that

$$\varepsilon_j < \frac{1}{t_s}(2 - t_s q_j)\left|S_j(k)\right|. \quad (32)$$

If we take $\varepsilon_j = \left|S_j(k)\right|/2$ and the sampling time meets the requirement of $t_s < 4/(1+2q_j)$, Eq. (32) can be guaranteed. The hyperbolic tangent function $\tanh(S_j(k)/\sigma_j)$ is used to replace the sign switching function $\mathrm{sgn}(S_j(k))$ in Eq. (28) to avoid the chattering effects in practical implementation. Here, σ_j is the boundary layer thicknesses.

3.2 Lateral Tire Force Estimation

According to the control low designed in Eq. (28), tire forces are critical to accomplishing the control target. Tire forces are hard to measure directly by sensors in practice. Analytical estimation is a practical way to obtain real-time tire forces and tire-road adhesion information [22, 23]. Based on the Dugoff tire model introduced in Section 2, an unscented Kalman filter is employed to estimate the real-time tire forces. According to the Dugoff tire model, the factors that determine the tire forces are road adhesion coefficient, tire vertical load, tire lateral stiffness, tire side-slip angle, and wheel slip ratio. Among all these factors, the road adhesion coefficient is the only one that can not be measured or calculated directly. Here we define nominal longitudinal and lateral tire forces F_{xi}^0 and F_{yi}^0 to describe the computable part of them, which are expressed as

$$\begin{cases} F_{xi}^0 = F_{zi} k_x \dfrac{\lambda_i}{1+\lambda_i} f(L_i), \\ F_{yi}^0 = F_{zi} k_y \dfrac{\tan\alpha_i}{1+\alpha_i} f(L_i). \end{cases} \quad (33)$$

Then the measurement equations used for estimating are derived as

$$\begin{cases} a_x = \dfrac{1}{m}(\mu_{fl}F_{xfl}^0 + \mu_{fr}F_{xfr}^0 + \mu_{rl}F_{xrl}^0 + \mu_{rr}F_{xrr}^0), \\ a_y = \dfrac{1}{m}(\mu_{fl}F_{yfl}^0 + \mu_{fr}F_{yfr}^0 + \mu_{rl}F_{yrl}^0 + \mu_{rr}F_{yrr}^0), \\ \dot{\gamma} = \dfrac{1}{I_z}(a(\mu_{fl}F_{yfl}^0 + \mu_{fr}F_{yfr}^0) - b(\mu_{rl}F_{yrl}^0 + \mu_{rr}F_{yrr}^0) \\ \quad + c(-\mu_{fl}F_{xfl}^0 + \mu_{fr}F_{xfr}^0 - \mu_{rl}F_{xrl}^0 + \mu_{rr}F_{xrr}^0)). \end{cases} \quad (34)$$

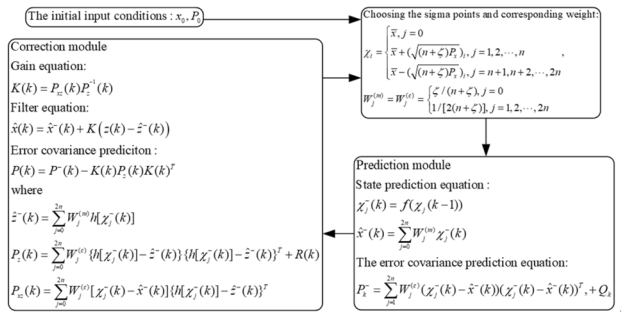

Figure 4 Procedure of UKF

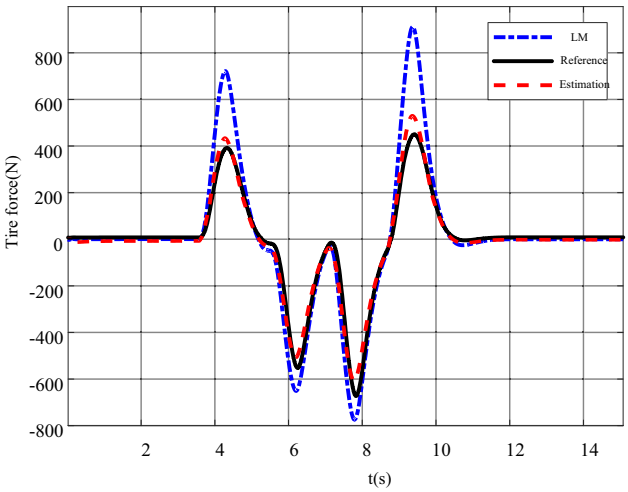

Figure 5 Lateral front left lateral tire force estimation results

The details of UKF are displayed in Figure 4, where system states are the four tire road adhesion coefficients, namely $\boldsymbol{x} = [\mu_{fl}, \mu_{fr}, \mu_{rl}, \mu_{rr}]^{\mathrm{T}}$; the inputs to the system are eight nominal ire forces, namely $\boldsymbol{u} = [F_{yfl}^0, F_{yfr}^0, , F_{yrl}^0, F_{yrr}^0, F_{xfl}^0, F_{xfr}^0, F_{xrl}^0, F_{xrr}^0]^{\mathrm{T}}$; the system outputs are $\boldsymbol{z} = [a_x, a_y, \dot{\gamma}]^{\mathrm{T}}$.

After obtaining the estimated road adhesion coefficients, the lateral tire forces can be calculated by the Dugoff model. The estimation results of the front left tire are shown in Figure 5.

In Figure 5, the blue curve is the tire force obtained by the linear tire model, which can be expressed as tire slip angle times tire lateral stiffness; the black curve is the reference value output by CarSim®; the red curve is the estimation result based on the method aforementioned. The result obtained by the linear model is larger than the reference because the lateral stiffness will decrease with the increase of the tire slip angle. It can be shown in Figure 5 that the estimation value matches the reference curve pretty well so it can be applied in the whole control strategy.

3.3 Optimal Energy Efficiency Torque Allocation

According to the former definition, the two virtual control inputs of the vehicle motion control are combinations of four IWM torque outputs. The optimal torque allocation is designed to complete the following tasks: ① minimizing the power consumption; ② satisfying the control requirements.

The inverter power consumption and the mechanical friction power consumption are considered uncontrollable, so the total power consumption can be described as

$$P_{con} = P_{out} + P_{iron} + P_{copper}, \tag{35}$$

where P_{out} is the motor mechanical output; P_{iron} is the motor iron loss; P_{copper} is the motor copper loss. More specifically,

$$\begin{aligned} P_{copper} &= R_a(i_d^2 + i_q^2) \\ &= R_a\left((i_{dt} - \frac{\omega_e L_q i_{qt}}{R_i})^2 + (i_{qt} + \frac{\omega_e(\varphi_f + L_d i_{dt})}{R_i})^2\right), \end{aligned} \tag{36}$$

$$\begin{aligned} P_{iron} &= R_i(i_{di}^2 + i_{qi}^2) \\ &= \frac{\omega_e^2 L_d^2 i_{qt}^2}{R_i} + \frac{\omega_e^2(\varphi_f + L_d i_{dt})^2}{R_i}, \end{aligned} \tag{37}$$

$$P_{out} = T_e\omega, \tag{38}$$

$$i_{qt} = \frac{T_e}{p_n\varphi_f}. \tag{39}$$

In Section 2, it is assumed that $L_d = L_q$. According to Ref [20],

$$i_{dt} = \frac{\omega_e^2 L_d(R_a + R_i)\varphi_f}{R_a R_i^2 + \omega_e^2 L_d^2(R_a + R_i)}. \tag{40}$$

Then the object function of motor power consumption is derived as

$$J_1 = \left\| \sum_{i=fl}^{rr} P_{con,i} \right\|^2. \tag{41}$$

The tire slip energy is considered to be important dissipation energy from driving axles to wheels [24]. To make the most use of driving torque, an objective function is introduced to minimize the tire slip energy, which is

$$\min J_2 = \|P_{tloss}\|^2 = \sum_{i=fl}^{rr} (T_i(k)\omega_i(k) - F_{xi}(k)v_x(k))^2. \tag{42}$$

Table 1 Vehicle parameters

Definition	Value
Vehicle total mass m(kg)	1259.98
Vehicle yaw moment of inertia I_z(kg·m^2)	4607
Distance from CG to front axle a(m)	1.14
Distance from CG to rear axle b(m)	1.64
Tire rolling radius R_w(m)	0.36
Cornering stiffness of the front tire k_1(N/rad)	− 143583
Cornering stiffness of the rear tire k_2(N/rad)	− 111200
Transmission ratio of steering system G_p	17
Wheel yaw moment of inertia I_w(N·m^2)	1.33
IWM control gain K_m(N·m/V)	80

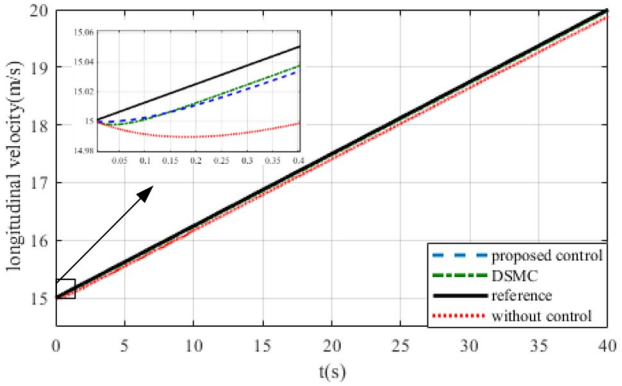

Figure 6 Simulation results of longitudinal velocity

The IWM can work in both driving and braking modes, while under certain conditions the IWM braking will not be enough. To fully use the braking recovery energy, a parallel braking energy recovery strategy based on feedback braking is applied where the mechanical braking system will start to work when the IWM braking force is saturated. This can be described as

$$T_t = \max\{-4T_{e\max}, u_1\}, \tag{43}$$

$$T_{bm} = u_1 - \max\{u_1, -4T_{e\max}\}, \tag{44}$$

where T_t is total torque provided by IWMs; $T_{e\max}$ is IWM output saturation; T_{bm} is braking torque provided by mechanical braking system.

IWM torque output T_e complies with its physical saturation, which is

$$-T_{e\max} \le T_e \le T_{e\max}, \tag{45}$$

$$T_{e\max}(\omega) = \begin{cases} T_{\max}, \text{ if } \omega \le P_{\max}/T_{\max}, \\ P_{\max}/\omega, \text{ else}, \end{cases} \tag{46}$$

where $P_{\max}$ and $T_{\max}$ are max power and max torque output of the IWM; ω is IWM rotational speed.

The first task can be accomplished by distributing the IWM torque to meet the following constraints:

$$\begin{cases} \Sigma T(k) = T_{fl}(k) + T_{fr}(k) + T_{rl}(k) + T_{rr}(k), \\ \Delta T(k) = -T_{fl}(k) + T_{fr}(k) - T_{rl}(k) + T_{rr}(k), \end{cases} \tag{47}$$

$$J_3(k) = (u_1(k) - \sum T(k))^2 + (u_2(k) - \Delta T(k))^2, \tag{48}$$

where J_3 is the motion control cost function, which is to convert the hard constraints in Eq. (47) into the soft constrain in Eq. (48).

Then the overall cost-function of the optimal allocation is defined as

$$J(k) = \xi_1 J_1(k) + \xi_2 J_2(k) + \xi_3 J_3(k), \tag{49}$$

where ξ_1, ξ_2 and ξ_3 are weights.

In summary, the optimal torque allocation problem can be reformulated as: minimizing the cost function Eq. (49) under the constraints of Eqs. (43)–(45).

This problem can be solved by the Sequential Quadratic Programming (SQP) proposed in Ref. [25] which can be summarized as follows. For optimal problem:

$$\begin{cases} \min & f(x), \\ \text{s.t.} & h_i(x) = 0, i \in E = \{1, 2, \ldots, l\}, \\ & g_i(x) \ge 0, i \in I = \{1, 2, \ldots, m\}, \end{cases} \tag{50}$$

The Lagrange function is defined as

$$L(x, \mu, \lambda) = f(x) - \sum_{i \in E} \mu_i h_i(x) - \sum_{i \in I} \mu_i g_i(x). \tag{51}$$

And then $\boldsymbol{A^E}(\boldsymbol{x}) = \nabla h(x)^{\mathrm{T}}$, $\boldsymbol{A^I}(\boldsymbol{x}) = \nabla g(x)^{\mathrm{T}}$, $\boldsymbol{A}(\boldsymbol{x}) = [A^E; A^I]$, $W(x, \mu, \lambda) = \nabla^2_{xx} L(x, \mu, \lambda)$.

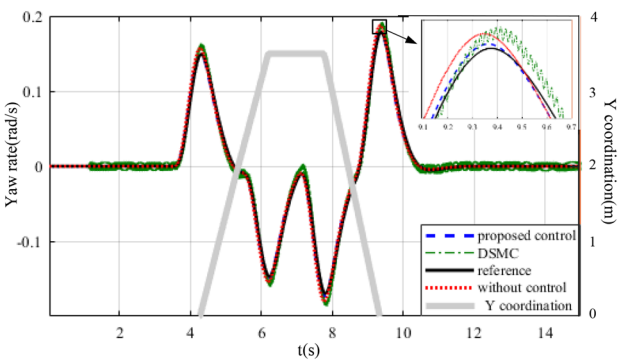

Figure 7 Simulation results of yaw rate

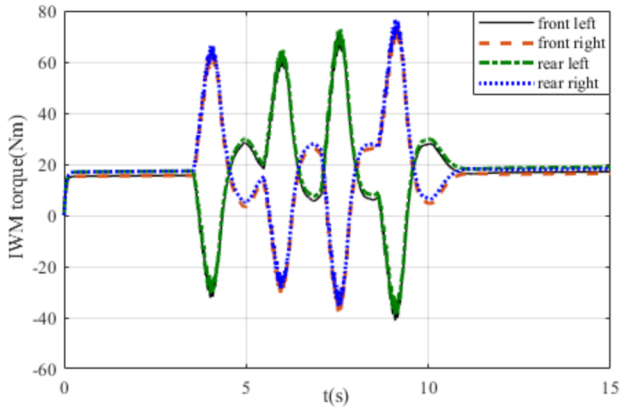

(a) Load based allocation

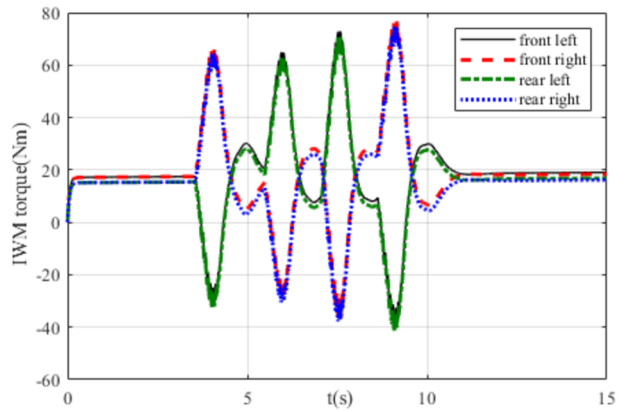

(b) Optimal allocation

Figure 8 Simulation results of IWM torques

Initialization step, given initial pair $(x_0, \mu_0, \lambda_0) \in \mathbb{R}^n \times \mathbb{R}^l \times \mathbb{R}^m$ and symmetric positive definite matrix $B_0 \in \mathbb{R}^{n\times n}$, calculate $\boldsymbol{A_0^E}(\boldsymbol{x}) = \nabla h(x_0)^{\mathrm{T}}, \boldsymbol{A_0^I}(\boldsymbol{x}) = \nabla g(x_0)^{\mathrm{T}}$, $A_0 = [A_0^E; A_0^I]$. Choose parameter $\eta \in (0, 1/2)$ and the allowable errors $0 \le \varepsilon_1, \varepsilon_2 \ll 1$. Set $k := 0$.

Step 1, solve the subproblem

$$\begin{cases} \min \ \frac{1}{2} d^{\mathrm{T}} B_k d + \nabla f(x_k)^{\mathrm{T}} d, \\ \text{s.t.} \quad h(x_k) + A_k^E d = 0, \\ \qquad g(x_k) + A_k^I d \ge 0, \end{cases} \tag{52}$$

to get the optimal solution d_k.

Step 2, if $\|d_k\|_1 \le \varepsilon_1$ and $\|h_k\|_1 + \|(g_k)_-\|_1 \le \varepsilon_2$, stop and get an approximate KT point of the original problem (x_k, μ_k, λ_k).

Step 3, for a certain cost function $\phi(x, \sigma)$, choose a penalty parameter σ_k to make d_k is in the falling direction of $\phi(x, \sigma)$ at the point of x_k.

Step 4, Armijo searching. Make m_k be the minimum nonnegative integer m satisfying the following inequality:

$$\phi(x_k + \rho^m d_k, \sigma_k) - \phi(x_k, \sigma_k) \le \eta \rho^m \phi'(x_k, \sigma; d_k), \tag{53}$$

then choose $\alpha_k := \rho^{m_k}, x_{k+1} := x_k + \alpha_k d_k$.

Step 5, calculate

$\boldsymbol{A_{k+1}^E} = \nabla h(x_{k+1})^{\mathrm{T}}$, $\boldsymbol{A_{k+1}^I} = \nabla g(x_{k+1})^{\mathrm{T}}$, $\boldsymbol{A_{k+1}} = [A_{k+1}^E; A_{k+1}^I]$ and the least-squares multiplier

$$\begin{bmatrix} \mu_{k+1} \\ \lambda_{k+1} \end{bmatrix} = [A_{k+1} A_{k+1}^{\mathrm{T}}]^{-1} A_{k+1} \nabla f_{k+1}. \tag{54}$$

Step 6, correct B_k to B_{k+1}. Set

$$\begin{aligned} s_k = \alpha_k d_k, y_k =& \nabla_x L(x_{k+1}, \mu_{k+1}, \lambda_{k+1}) \\ & - \nabla_x L(x_k, \mu_{k+1}, \lambda_{k+1}), \end{aligned} \tag{55}$$

$$B_{k+1} = B_k - \frac{B_k s_k s_k^{\mathrm{T}} B_k}{s_k^{\mathrm{T}} B_k s_k} + \frac{z_k z_k^{\mathrm{T}}}{s_k^{\mathrm{T}} z_k}, \tag{56}$$

where

$$z_k = \theta_k y_k + (1 - \theta_k) B_k s_k, \tag{57}$$

$$\theta_k = \begin{cases} 1, & f\ s_k^{\mathrm{T}} y_k \ge 0.2 s_k^{\mathrm{T}} B_k s_k, \\ \frac{0.8 s_k^{\mathrm{T}} B_k s_k}{s_k^{\mathrm{T}} B_k s_k - s_k^{\mathrm{T}} y_k}, & if\ s_k^{\mathrm{T}} y_k \ge 0.2 s_k^{\mathrm{T}} B_k s_k. \end{cases} \tag{58}$$

Step 7, update k as k+1, then switch to step 1.

4 Simulation Results and Analyses

Simulations are conducted to verify the effectiveness of the proposed control strategy based on the co-simulation platform of CarSim® and Matlab/Simulink. The model is established based on a high-fidelity full-vehicle model in

Table 2 Performances under different control strategies

	Error covariance of v_x	Error covariance of y	Power consumption
DSMC+LBA	$9.2134*10^{-4}$	$1.1064*10^{-4}$	$3.8009*10^{5}$
ADSMC+LBA	$4.1615*10^{-4}$	$5.3361*10^{-5}$	$2.6731*10^{5}$
ADSMC+OA	$4.5844*10^{-4}$	$5.7721*10^{-5}$	$2.2481*10^{5}$

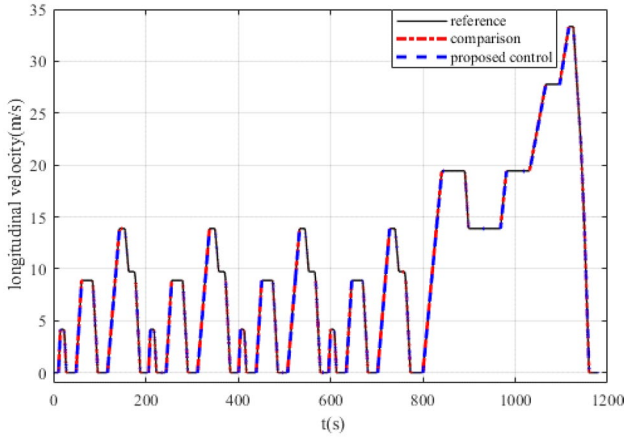

Figure 9 Simulation results of longitudinal velocity

CarSim® and all the powertrain components are replaced by four IWMs. Meanwhile, simulation results by the torque distribution method shown in Eq. (59) are used as comparisons to validate the improvement of integrated optimal torque allocation. The parameters of the vehicle used in simulations are shown in Table 1.

$$\begin{cases} T_{fld} = \dfrac{b}{2(a+b)} \sum T - \dfrac{1}{4}\Delta T, \\ T_{frd} = \dfrac{b}{2(a+b)} \sum T + \dfrac{1}{4}\Delta T, \\ T_{rld} = \dfrac{a}{2(a+b)} \sum T - \dfrac{1}{4}\Delta T, \\ T_{rrd} = \dfrac{a}{2(a+b)} \sum T + \dfrac{1}{4}\Delta T. \end{cases} \tag{59}$$

Double line change and new European driving cycle (NEDC) are conducted in simulations to verify the motion control performance and the economic efficiency of the proposed control. The results are shown in the subsequent sections.

4.1 Double Line Change

The control target of this study is to coordinate the motion control of EVs driven by IWMs in an effective way. The first simulation is the double line change with longitudinal velocity increase. The vehicle is set to accelerate from 15 to 20 m/s in 40 s and the double line change track is shown below. The air density is set as 1.206 kg/m^3 during the simulation. Two comparison simulations are also conducted; one is conducted by using the normal sliding mode control with proposed torque optimal allocation, and the other is conducted by using the DASMC and the allocation method based on tire load. Simulation results are displayed in Figures 6 and 7.

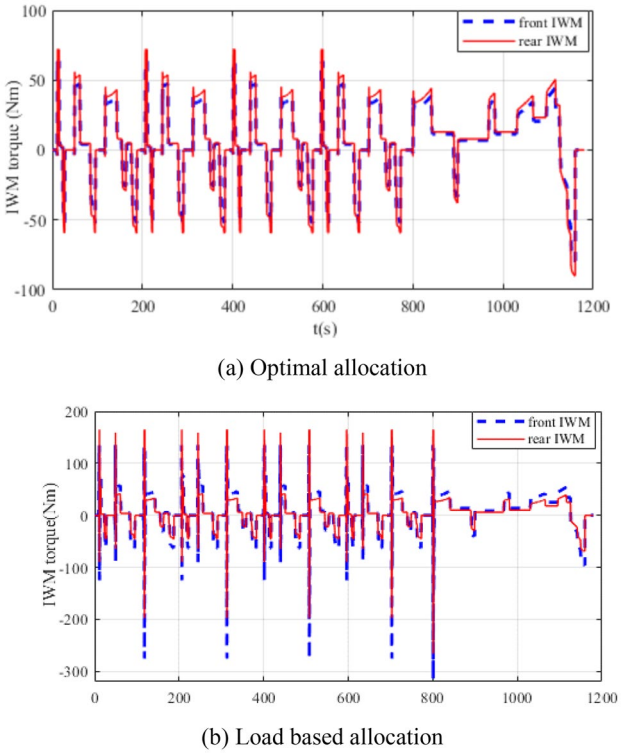

Figure 10 Simulation results of total power consumption

From Figures 6 and 7, it can be concluded that the proposed control method can accomplish the longitudinal and yaw motion control successfully. Moreover, the ADSMC outperforms the DSMC in suppressing chattering according to Figure 7.

The load-based allocation (LBA) method in Eq. (50) is applied as a comparison to the optimal allocation (OA) method. The results are shown in Figure 8.

In Figure 8, it can be seen that the yaw motion control is accomplished by differential torques between left

Table 3 Performances under different allocation methods

	Error covariance of v_x	Maximum absolute tracking error of v_x	Power consumption	Energy efficiency(%)
ADSMC+LBA	$8.5844*10^{-4}$	0.3423	$3.6731*10^5$	67.9
ADSMC+OA	$1.36*10^{-2}$	0.4960	$3.2481*10^5$	73.6%

and right IWMS in both two allocation methods. While the allocation ratios between front and rear IWMs are different. To quantitatively illustrate the improvement of the proposed control strategy more specifically, Table 2 shows the performances under different control strategies.

The evaluation results are obtained based on the aforementioned simulations. It can be concluded that with the ADSMC, the tracking performance has been improved compared with the DSMC for its better chattering suppression performance. Furthermore, the power consumption is also decreased by ADSMC according to Table 2, because the frequent torque changes will cause more power consumption. According to the second and third rows of Table 2, the power consumption by OA is decreased as expected but the tracking performances of yaw rate and longitudinal velocity are slightly worse than LBA. Combining with the Eqs. (48)–(50), it can be concluded that the OA sacrifices the tracking performance to obtain lower energy consumption.

4.2 NEDC

Although the above simulation results can verify the coordinated motion control of the proposed control strategy, they are still not enough to demonstrate energy efficiency in such a short time interval. To fully prove the control performance of the proposed strategy, the NEDC is conducted. The vehicle is set to drive in a single line without steering. Similarly, simulations using the abovementioned control strategy ADSMC+LBA are conducted as the comparisons. The simulation results are shown in Figures 9 and 10. The control performance is displayed in Table 3.

In Figure 9, it can be seen that both control strategies can track the reference longitudinal velocity in the whole-time range. While in Figure 10, the torque outputs with OA meet the torque output limit requirement and also have fewer sharp changes. According to Table 3, the control strategy with LBA shows better tracking performance at the cost of more power consumption and less energy efficiency. While even the control strategy with OA shows a bigger tracking error, it is still effective for the maximum absolute tracking error is 0.4960 which is totally acceptable. This indicates that the proposed control strategy can generate a proper control input to the system in an energy-efficient way, precisely to track the reference outputs to accomplish vehicle-coordinated motion control.

Based on all the simulation results exhibited above, the effectiveness of such an energy-efficient control strategy for EVs driven by IWMs based on DASMC is demonstrated.

5 Conclusions

An energy-efficient control strategy for EVs driven by IWMs based on DASMC is proposed in this study. Models are established firstly to demonstrate the operation mechanism of the whole system and two virtual control variables are used to describe the longitudinal and yaw control efforts to complete the vehicle coordinate motion control. Then DASMC method is applied to calculate the required total driving torque and yaw moment. A tire force estimator using UKF is designed to estimate real-time lateral tire forces used in the control scheme. Based on all the abovementioned factors, energy efficient torque allocation method is developed to distribute the total driving torque and differential torque to each IWM. Simulation results of the proposed control strategy using the co-platform of Matlab/Simulink and CarSim® demonstrate that this study can accomplish the vehicle motion control in a coordinated and economic way and improve the tracking performance as well as the system robustness.

Acknowledgements
Not applicable.

Author Contributions
WZ and CW were in charge of the whole trial; HZ wrote the manuscript and executed the research plan; CZ assisted with data processing and analyses. All authors read and approved the final manuscript.

Authors' Information
Han Zhang received her PhD degree in vehicle engineering from *Nanjing University of Aeronautics and Astronautics, China,* in 2020. She is currently a lecturer with the *Department of Vehicle Engineering, Nanjing University of Aeronautics and Astronautics, China*. Her research interests include vehicle system dynamics and control systems.
Changzhi Zhou is currently a master candidate at *Department of Vehicle Engineering, Nanjing University of Aeronautics and Astronautics, Nanjing, China.*
Chunyan Wang, received the PhD degree in mechanical engineering from *Jilin University, China*, in 2008. She is currently a Professor and the director with the *Department of Vehicle Engineering, Nanjing University of Aeronautics and Astronautics, Nanjing, China*. Her research interest includes vehicle system dynamics.
Wanzhong Zhao received the PhD degree in vehicle engineering from *Beijing Institute of Technology, China*, in 2009. He is currently a professor in the *Department of Vehicle Engineering, Nanjing University of Aeronautics and Astronautics, China.* His research interests include vehicle system dynamics.

Funding
Supported by Jiangsu Provincial Key R&D Plan (Grant No. BE2022053), Youth Fund of Jiangsu Provincial Natural Science Foundation (Grant No. BK20200423) and National Natural Science Foundation of China (Grant No. 5210120245).

Availability of Data and Materials
The datasets supporting the conclusions of this article are included within the article.

Declarations

Competing Interests
The authors declare no competing financial interests.

Received: 16 December 2021 Revised: 17 March 2023 Accepted: 23 March 2023
Published online: 28 April 2023

References

[1] Shuai Zhang, Mingzhou Chen, Wenyu Zhang. A novel location-routing problem in electric vehicle transportation with stochastic demands. *Journal of Cleaner Production*, 2019, 221: 567-581.
[2] C Lv, Y Liu, X Hu, et al. Simultaneous observation of hybrid states for cyber-physical systems: A case study of electric vehicle powertrain. *IEEE Transactions on Cybernetics*, 2018, 48(8): 2357 - 2367.
[3] Lei Zhang, Zhiqiang Zhang, Zhenpo Wang, et al. Chassis coordinated control for full x-by-wire vehicles-A review. *Chinese Journal of Mechanical Engineering*, 2021, 34: 42.
[4] C Pan, L Chen, L Chen, et al. Research on motor rotational speed measurement in regenerative braking system of electric vehicle. *Mechanical Systems & Signal Processing*, 2015, 66(2): 829-839.
[5] B Li, H Du, W Li. Fault-tolerant control of electric vehicles with in-wheel motors using actuator-grouping sliding mode controllers. *Mechanical Systems & Signal Processing*, 2016, s72–73: 462-485.
[6] Y Wang, H Fujimoto, S Hara. Driving force distribution and control for EV with four in-wheel-motors: A case study of acceleration on split-friction surfaces. *IEEE Transactions on Industrial Electronics*, 2017, 64(4): 3380-3388.
[7] D B Lu, M G Ouyang, J Gu, et al. Instantaneous optimal regenerative braking control for a permanent-magnet synchronous motor in a four-wheel-drive electric vehicle. *Proceedings of the Institution of Mechanical Engineers, Part D: Journal of Automobile Engineering*, 2014, 228(8): 894-908.
[8] W Z Zhao, C Y Wang, P K Sun, et al. Integration optimization of differential assisted steering of electric vehicle with motorized wheels based on quality engineering. *Science China (Technological Sciences)*, 2011, 54(11): 3047–3053.
[9] Yunwu Li, Xueyan Huang, Dexiong Liu, et al. Hybrid energy storage system and energy distribution strategy for four-wheel independent-drive electric vehicles. *Journal of Cleaner Production*, 2019, 220: 756-770.
[10] C Hu, R Wang, F Yan, et al. Robust composite nonlinear feedback path-following control for independently actuated autonomous vehicles with differential steering. *IEEE Transactions on Transportation Electrification*, 2016, 2(3): 312-321.
[11] Y P Yang, C P Lo. Current distribution control of dual directly driven wheel motors for electric vehicles. *Control Engineering Practice*, 2008, 16(11): 1285-1292.
[12] M Demirci, M Gokasan. Adaptive optimal control allocation using Lagrangian neural networks for stability control of a 4WS–4WD electric vehicle. *Transactions of the Institute of Measurement and Control*, 2013, 35(8): 1139-1151.
[13] D Wu, H Ding, K Guo, et al. Stability control of four-wheel-drive electric vehicle with electro-hydraulic braking system. *SAE*, 2014-01-2539, 2014.
[14] Y Li, J Zhang, K Guo, et al. A study on force distribution control for the electric vehicle with four in-wheel motors. *SAE*, 2014-01-2379, 2014.
[15] X Zhang, K Wei, X Yuan, et al. Optimum torque distribution for stability improvement of four-wheel distributed driven electric vehicle using coordinated control. *Journal of Computational and Nonlinear Dynamics*, 2016, 11(5): 051017.
[16] Y Wang, H Fujimoto, S Hara. Torque distribution-based range extension control system for longitudinal motion of electric vehicles by LTI modeling with generalized frequency variable. *IEEE/ASME Transactions on Mechatronics*, 2016, 21(1): 443-452.
[17] Y Li, J Zhang, C Lv, et al. Coordinated control of the steering system and the distributed motors for comprehensive optimization of the dynamics performance and the energy consumption of an electric vehicle. *Proceedings of the Institution of Mechanical Engineers, Part D: Journal of Automobile Engineering*, 2017, 231(12): 1605-1626.
[18] H Zhang, W Zhao, J Wang. Fault-tolerant control for electric vehicles with independently driven in-wheel-motors considering individual driver steering characteristics. *IEEE Transactions on Vehicular Technology*, 2019, 68(5): 4527-4536.
[19] L Chen, M Bian, Y Luo, et al. Maximum tire road friction estimation based on modified dugoff tire model. *2013 International Conference on Mechanical and Automation Engineering*, Jiujang, 2013: 56-61.
[20] S Morimoto, Y Tong, Y Takeda, et al. Loss minimization control of permanent magnet synchronous motor drives. *IEEE Transactions on Industrial Electronics*, 2002, 41(5): 511-517.
[21] Jinkun Liu. Sliding mode control design and matlab simulation. Beijing: Tsinghai University Press, 2005. (in Chinese)
[22] Yan Wang, Chen Lv, Yongjun Yan, et al. An integrated scheme for coefficient estimation of tire–road friction with mass parameter mismatch under complex driving scenarios. *IEEE Transactions on Industrial Electronics*, 2022, 69(12): 13337-13347.
[23] Yan Wang, Jingyu Hu, Faan Wang, et al. Tire road friction coefficient estimation: review and research perspectives. *Chin. J. Mech. Eng.*, 2022, 35: 2.
[24] B Zhao , X Nan , C Hong , et al. Stability control of electric vehicles with in-wheel motors by considering tire slip energy. *Mechanical Systems and Signal Processing*, 2019, 118: 340-359.
[25] Jorge Nocedal, Stephen J Wright. *Numerical optimization*. New York: Springer, 2006.